Ternary β and γ phases in the Al-Au-Cu system at 750˚C

V.K. Bhatia[a], C.S. Kealley[a], R. Wuhrer[b], K.S. Wallwork[c], M.B. Cortie[a*]

[a]Institute for Nanoscale Technology, University of Technology Sydney, PO Box 123, Broadway, NSW, 2007, Australia

[b]Microstructural Analysis Unit, University of Technology Sydney, PO Box 123, Broadway, NSW, 2007, Australia

[c]Australian Synchrotron, 800 Blackburn Road, Clayton, Victoria 3168, Australia

Corresponding Author - Tel: +612-9514-2208, Fax:+612-9514-2219

Email: michael.cortie@uts.edu.au

Abstract

There are many aspects of the phases and phase boundaries of the Al-Au-Cu ternary system that are still unknown. Although a 500˚C isothermal section and an 18 karat pseudobinary have been reported, many of the other constitutive relationships within the ternary are uncertain. Another unresolved issue is the range of compositions that can possibly serve as shape memory alloys. Here we investigate the constitutive relationships in this system at 750˚C. We confirm that the γ and β phases extend deep into the ternary but that the other known compounds are largely confined to the binary edges. The suitability of β-phase compositions of lower Au content for shape memory service is established.

Keywords: (A) metals and alloys, (C) shape memory, (C) phase diagrams, (D) scanning electron microscopy, SEM

1. Introduction

Both the structure and the physical properties of shape memory alloys (SMAs) have been extensively studied [1]. This has enabled a wide range of uses for these materials, with applications ranging from under-wires of bras to arterial stents and intricate jewellery [2-6]. However, there are some limitations due to the fact that many SMAs suffer from aging and martensite stabilization [7-9]. Both phenomena cause the transformation temperatures of the

SMA to change over time if it is left in one state for a long period or if it is exposed to elevated temperatures. These changes in transformation temperature generally restrict the usage of SMAs to applications where there is a significant difference between the operational and the transformation temperature so that switching can be guaranteed.

Another possible limiting factor is decomposition of the microstructure of the SMA [9-11]. This decomposition occurs because the parent β-phase of the SMA is generally metastable at room temperature. This means that in order to acquire these alloys in the β-phase at room temperature, they must first be annealed into the β-phase ('betatised') at some minimum elevated temperature at which the β-phase is stable, and then quenched. Since the decomposition of the β-phase into equilibrium phases requires thermally activated diffusive processes, decomposition at room temperature is exceedingly slow, even negligible. However, if the application of the SMA requires an operating temperature intermediate between room temperature and the betatising temperature, then there may be sufficient thermal energy to activate diffusive processes and the β-phase may start to decompose. As the β-phase is destroyed, it will lose its shape memory properties. The decomposition phenomenon is well-known in diverse range of Cu-base β-phase SMAs and has also been reported in Au-based β-phase materials, such as Au-Cu-Zn [12] (in which ageing of the $L2_1$ phase eventually caused the precipitation of α-(Au,Cu)) and $AlAu_2Mn$, which orders first from $B2 \rightarrow L2_1$ and then, during ageing, forms precipitates of Al_2Au [13].

One alloy that resists these problems is Spangold, a SMA with a nominal composition of $Au_7Cu_5Al_4$, which makes it an 18 karat gold [2]. While the 18 K aspect gives Spangold some potential for use in the jewellery industry, for technological applications the attribute of greater interest is that it appears to be relatively resistant to both decomposition and aging [14,15]. Spangold has many other properties that could make it useful as a shape memory alloy, including good castability, high strength and wear resistance, and good resistance to corrosion [16,17]. Also, it has two fundamental properties that make it ideal for use in biomedical implant applications: gold is biocompatible [18] and is radio-opaque due to its high atomic number (the latter feature facilitates the positioning or manipulation of a medical device *in vivo*) [19]. The major drawback of this material, however, is the 76 wt.% gold it contains, which would make the manufacturing cost high. For applications such as micro-actuators, small electronic devices and small medical components this should not pose much of a problem, however if this material was to be used in larger devices then the manufacturing cost would prove to be too high no matter how well the alloy would work. This raises the question of whether the stability and resistance to aging of Spangold might also be found in Al-Au-Cu β-phase alloys of lower Au content. Previous work in this system has been focussed on the 500˚C isothermal section and on 18 K compositions [20,21]. The focus of the present work was, however, to establish the boundaries of the β-phase at lower Au contents and at 750˚C, which is a more realistic betatising temperature for the lower karat compositions.

2. Experimental Procedures

The samples for this project were manufactured using high purity base metals of Au (99.99%), Cu (99.9%) and Al (99.99+%) melted in an alumina crucible under a protective layer of carbon pellets. Table 1 provides the list of compositions. The Au was melted first, and then the Cu and Al stirred in. The samples were annealed at 750°C to convert them into β-phase, followed by quenching into iced brine. This was expected to freeze in the β-phase that formed during the annealing, by analogy with the situation pertaining to Cu_3Al, Cu_xSn, Cu_xZn, and other shape memory alloys. Of course, if the martensite start temperature (M_s) of the sample had been above 0˚C, then the sample would additionally be in the martensitic form after this treatment.

Samples were cut up using a low speed Leco saw, taking care to avoid over-heating. Differential scanning calorimetry (DSC) analyses were performed using a Thermal Analysis DSC 2920. A ramp rate of 10 °C/min was used. A Zeiss Supra 55 VP scanning electron microscope (SEM) was used at 20 keV in high current mode with a 120 μm aperture in back-scatter mode to verify the composition and phase relationships. An Oxford Pentafet energy dispersive spectroscopy (EDS) system attached to the microscope was used for EDS analysis. A Cu standard was used to calibrate the EDS system and for quantitative optimisation. The EDS analyses reported here are each the result of averaging five measurements and are expected to be accurate to within 0.5%. Optical microscopy on an Olympus BH2 equipped with a JVC TK-1280E digital camera was used to examine polished and etched samples using ordinary light and polished samples using Nomarski interference contrast (the latter is very sensitive to surface relief). Ferric chloride solution was found to be a suitable etchant.

3. Results and Discussion

The composition of all discernable phases after annealing was determined by EDS and is shown in Table 1. From previous knowledge [20] and the characterisation results shown below, the thirteen samples can be classified according to how much of the phases α, β, γ or Al_2Au they contain. The α-phase is the face-centred cubic solid solution of Au and Cu, also denoted as (Au,Cu). The β-phase is an electron compound packed on a body-centred cubic scheme and is the parent phase of most non-ferrous shape memory alloys. The γ-phase is a hard, brittle electron compound of complex structure. Finally, Al_2Au, also known as 'purple gold', is a purple-colored intermetallic compound. Consideration of the microstructures, compositions and electron-to-atom (e/a) ratios of the experimental samples, taken together with the published binary edge phase diagrams [12,22], 500˚C isothermal section [20] and 18K pseudobinary [21], permitted the construction of a 750˚C isothermal section, Figure 1. We will now briefly discuss the main features of this ternary section, and justify its construction.

3.1 α-phase

Sample 6, which had a nominal 30 at.% Au, contained cored dendrites of α-phase (e/a= 1.28), with some gold-rich interdendritic β-phase (e/a = 1.40) in the as-cast condition, Figure 2(a) and

(b). However, after annealing it is a substantially α-phase material (*e*/*a* =1.30). Therefore, there is a peritectic relationship in this system, with the solidification occurring first as L (liquid) →L+α and then, once the composition of the remaining liquid has become enriched in Al, L+α→β. This is similar to the situation reported previously for the 50 at.% Au region of the phase diagram [21]. Overall, the Sample 6 composition lies within the α-phase field of the previously published 500˚C isothermal section [20], which is continuous along the Au-Cu edge at that temperature. It should also be continuous at 750 °C. Thermal analysis revealed that the liquidus and solidus were 890 and 834˚C on cooling, compared to ~935˚C and ~925˚C respectively for a binary alloy with the same ratio of Au to Cu. Therefore, the addition of 15 at% Al has suppressed the melting point by 45˚C and widened the melting range.

The α-phase in this region of the phase diagram can order at lower temperatures to form the compound Cu_3Au. There is a small exothermic signal at ~320˚C in the DTA scan of Sample 6, cooled at 10˚C per second, evidently generated by the α-(Cu,Au,Al)→ Cu_3Au ordering reaction. However, the strong characteristic superlattice {100} and {110} peaks for Cu_3Al were absent in the XRD patterns which had been taken on samples annealed at 750˚C and then *quenched*. These samples showed only the peaks expected for α-(Au,Cu) plus some evidence for a small proportion of a second phase, possibly the β-phase. Evidently, quenching suppressed the ordering reaction, as in the case of α-(Au,Cu)→AuCu [23]. The α-(Cu,Au,Al)→Cu_3Au transformation occurred about 20˚C higher than that of a binary (Au,Cu) alloy of the corresponding Au:Cu ratio, indicating that the addition of 15 at% Al raised the ordering temperature. This should be contrasted to the findings of Chapman and Gillam who reported that the addition of as little as 1.3 at.% Al to Cu_3Au *lowered* the transformation temperature by 40˚C [24]. Further investigation of the region between 1.3 and 15 at.% Al seems worthwhile.

Sample 7 should have had a dual phase α+β structure. As cast, it showed Widmanstätten needles of α (*e*/*a* ~1.35) in a matrix of β (*e*/*a* ~1.43), Figure 3(a). Typically, Widmanstätten needles of α grow at roughly 600˚C in the β-phase of coinage metal alloys that have been cooled across the β / (α+β) phase boundary. Naturally, the occurrence of this transformation is predicated on the width of the β-phase field reducing as the temperature falls. Therefore, Sample 7 was not only mostly comprised of β-phase at some higher temperature, but it is also clear that its β-phase field would have a V-shaped cross-section on a isopleth drawn across the ternary from the (Au,Cu) edge in the direction of increasing *e*/*a* ratio. Thermal analysis, placed the liquidus and solidus at about 899 and 868˚C respectively. There are exothermic signals on the cooling curve at 657˚C and then 580˚C, evidently corresponding to the start and end of α-phase formation respectively. The heating curve shows a single strong peak at 607˚C for the α+β→β reaction. There are further transformations in the vicinity of 350-400˚C but these are due to the martensitic transformation within the remaining β-phase, and will be discussed later. After annealing at 750˚C, followed by quenching, Sample 7 underwent an intergranular precipitation of a fine-scale duplex-structured bainite, Figure 3(b). These in turn consist of small regions of a dark-etching phase of relatively light average atomic number surrounded by a continuous phase of a heavier atomic number, Figure 3(c) and 3(d). However, the two phases are fine-scale and close in composition, making accurate EDS analysis of the individual regions problematic. The bainite nucleated and grew from grain boundaries and intra-granular nucleating sites in a feather-like fashion. XRD showed that

the sample contained both the peaks of the pure β-phase sample (Sample 8) nearby and of α-phase. Very simular microstructures have been observed when Cu-base β-phases decompose *e.g.* ref.[25].

The α-phase field in Figure 1 was drawn by combining the binary edge data, the isopleth of Levey, and the present analyses and observations.

3.2 β-phase

Coinage metal SMAs require a β-phase parent [1,26], so determination of the boundaries of this phase was a most important area of focus for the present work. Samples 8, 10, 11 and 13 were found to lie within the β-phase field at 750˚C. They were readily differentiated from the γ-phase alloys (see later) by their yellow colour and were also less brittle. For example, unlike γ-phase alloys, they could survive being dropped onto a hard surface. Nevertheless, the β-phase samples were still considerably harder and less ductile than the α-phase. In order to prove that the transformations observed by the DSC were indeed due to the martensitic phase transformation, images were taken using Nomarski interference optical microscopy. It is well known in the field that when a shape-memory alloy with a polished surface undergoes a transformation, laths will appear on the surface due to the strain in the lattice causing the surface to buckle [27]. These laths are easily seen under Nomarski interference conditions and generate bright changes in colour. In order to exploit this, samples were polished *e.g.* Figure 4(a), after which they were heated past their austenite transformation point and then cooled back through their martensite transformation temperature, Figure 4(b). The appearance of large numbers of laths across the surface indicated that the samples had undergone the shape-memory transformation.

The β-phase field in Figure 1 was drawn by starting from the Al-Cu binary [22], plotting the measured limiting compositions of β-phase at 750 °C, and extending the phase boundaries along lines of constant *e*/*a* ratio. This approach is equivalent to giving the β-phase a nominal stoichiometry of $Au_{8-x}Cu_{4+x}Al_4$, where for example in Spangold $x \approx 1$. The Cu-rich boundary of this phase field was less well-defined than the Al-rich edge, as the dual phase (α+β) field is very narrow and there was only one sample that ended up being located in it. However, EDS measurements indicated that the boundary of the β-phase field on the γ side was at an *e*/*a* ratio of about 1.46 at 750˚C. Finally, from the published 18K isopleth [21] it is known that, at 750˚C, the material would be partially molten, and the range of solid β-phase must therefore transition into (L+β), (L+β+γ), and (L+β+α) phase fields on the 750˚C isothermal section. The β-phase of the Au-Al binary phase diagram, which actually has the approximate stoichiometry Au_9Al_2 (rather than Au_3Al), has a eutectic with Au_8Al_3 at 525˚C and a peritectic with L and α at 545˚C, so it is clear that the β-phase stoichiometries for $0<x<1$ in $Au_{8-x}Cu_{4+x}Al$ will be completely molten on the 750˚C isothermal section. The measured melting points of the β-phases in this system are plotted in Figure 5(a). At 750˚C Spangold ($Au_7Cu_5Al_3$) is partially molten. Battezatti found the solidus at 726˚C and liquidus at 767˚C [28] while Levey *et al.* determined these to be in the vicinity of 736 and 775˚C respectively. The application of *in situ* X ray diffraction using synchrotron radiation provided further insight into the melting phenomena. For example, the profile of the

{011} peak of the β-phase is plotted for temperatures between 650˚C and 800˚C in Figure 5(b). The peaks start to disappear at about 731˚C, indicating the onset of melting. The last vestiges of solid phase disappeared at about 800˚C. Once melting begins the peak shifts to the right, indicating a decrease in lattice parameter. From Figure 5(a) it can be seen that the equilibrium Au content in β-phase decreases as the temperature rises. In this case the solid material must contain an increasingly greater proportion of Cu (metallic radius 0.128 nm, compared to the 0.144 nm of Au) as the temperature rises, and the lattice of the phase in equilibrium with the melt must therefore contract, as observed. There is no α-phase in these patterns indicating that in Spangold itself the reaction is β→(L+β)→L as the temperature is increased, as indeed was shown on the previously published 18 karat pseudobinary [21]. The approximate proportion of phases present in the melting zone can be obtained by plotting the normalised {011} peak area against temperature and taking this parameter to be proportional to the fraction of solid phase present, Figure 5(c). At 750˚C this sample consists of approximately 33% solid β-phase and 67% liquid, by mass.

X-ray diffraction at room temperature of all the β-phase samples indicated that they were in the low-temperature (martensitic phase), the structure of which has not been fully resolved. Evidently, the β-phase had transformed to martensite at some temperature above room temperature. In fact, the β→martensite and martensite→β transformations are evident on differential scanning calorimetry scans, Figure 6(a). The β→martensite transformation temperatures in this system are invariably about 50 or 60˚C lower than the reverse transformations. For example, Sample 10 ($Au_{6.9}Cu_{5.7}Al_{3.4}$), which had the lowest transformation temperatures, A_s was at ~88˚C and M_s at ~26˚C. The M_s is within the known range for Spangold but the A_s is a little higher than the ~78-85˚C usually reported for that alloy [14,29]. The small difference may have been caused by the slightly lower *e*/*a* ratio of Sample 10 relative to standard Spangold (1.42 *vs.*1.48). This parameter has an effect on transformation temperatures, and a drop in *e*/*a* (*ie.* a lowered Al content) is associated with a rise in transformation temperatures [1]. Sample 11 ($Au_{5.8}Cu_{6.7}Al_{3.5}$, *e*/*a*=1.43) manifested a broad and poorly defined transformation endotherm at about 268˚C. However, on cooling, the sample exhibited a classic martensite transformation peak at 175 °C. Furthermore, this process was repeatable. Therefore, the only possible origin for the endotherm at 268˚C was the martensite to austenite transformation. Sample 8 ($Au_{4.6}Cu_{7.9}Al_{3.5}$, *e*/*a*=1.44) also showed transformations at quite high temperatures with an obvious austenite transformation peak occurring at 357°C and a martensite transformation occurring at 329°C. These transformations are much closer to the standard type of peaks seen in many other shape memory alloys [1]. Curiously, Sample 13, (Cu_3Al, *e*/*a*=1.46) did not show any transformations, despite β-Cu_xAl being the basis of a well-known shape memory alloy. From the EDS analysis, the composition of this alloy was found to be Cu-23 at.% Al. Correlating this with the Cu-Al binary diagram [22] , it can be seen that this alloy is in the middle of the β-phase when annealed at 750 °C. However, the temperature of the martensite and austenite transformations is dependant on the Al content, ie. *e*/*a* ratio, and would be close to 390°C for this composition [1]. Therefore, when the sample was actually ramped through this temperature the martensite transformation was not recorded due to other enthalpy changes that occurred. The interfering reaction is most likely the decomposition of the β-phase into α+γ. This destroys the β-phase and its shape memory properties, explaining why there is no martensite transformation upon

subsequent cooling. Actually, this decomposition is a well documented process in Cu-base β-phases, e.g. [25] and is their main drawback. However, it appears not to occur in Spangold, at least over timescales of a few hours or so, and this is one of the main advantages that it has over the Cu-based alloys.

One trend that has been noted here (and in the literature [15]) is the increase in austenite transformation temperature with decreasing percentages of Au, Figure 6(b). This change is in addition to the effect of the *e*/*a* ratio on transformation temperature. The β-phase component of Samples 9 and 12 (which were mixed γ- and β -phase) also showed a martensitic transformation during thermal analysis. However it should be noted that the β-phase of Sample 12 decomposed when reheated in the DSC or DTA. In this respect, it was more like the Cu_3Al β-phase (*ie*. Sample 13), which readily undergoes eutectoid decomposition to α+γ, than like Spangold, which is resistant to such a process.

3.3 γ-phase

Application of metallography and X-ray diffraction indicated that Samples 1, 2 and 5 were almost entirely comprised of the γ-phase, Figure 7(a), with a lattice parameter that increased linearly as Au (metallic radius 0.144 nm) was substituted for Cu (metallic radius 0.128 nm), Figure 7(b). This trend suggests a formula $Al_4Au_xCu_{9-x}$ for the γ-phase in this system, with a lattice parameter of 0.8704 nm for $Al_4Au_0Cu_9$, increasing to 0.9175 for $Al_4Au_{5.3}Cu_{3.7}$. Samples 1, 2 and 5 also shared very similar characteristics, being extremely brittle and silver-white in colour.

Samples 3 and 4 were dual phase consisting of γ and Al_2Au (purple gold). Tie lines could be established for Sample 4, the microstructure of which is shown in Figure 8(a), and the Al_2Au phase in that sample could also be readily identified by optical microscopy of polished sections on account of its purple colour. In contrast, the patches of γ+Al_2Au eutectic in Sample 3 were too fine in scale for analysis of individual components, and in any case the Al_2Au in that sample largely dissolved into the γ matrix on annealing at 750˚C. Differential thermal analysis, Figure 8(b), clearly indicated both the solidification of the γ-phase and the formation of the Al_2Au+γ eutectic at about 800˚C. Prolonged annealing at a temperature below the eutectic evidently spheroidises the Al_2Au lamellae, Figure 8(c). In contrast, Samples 9 and 12 were dual phase consisting of dendrites of γ in a matrix of β, Figure 8(d). These two phases were very hard to differentiate by optical microscopy until the sample was etched with ferric chloride solution, after which they displayed a large difference in colour and contrast. However, when a polished section of these samples was imaged in the SEM under backscatter conditions there was little contrast, indicating that the two phases did not differ much in average atomic mass.

It is known from the binary Al-Cu diagram [22] that the γ-phase exists between 63 and 69 at.% Cu at 750°C, *ie*. between *e*/*a* ratios of 1.62 and 1.74. This was used as the starting point for drawing the γ-phase in the isothermal section. The phase was then extended towards the Al-Au edge by linking the edges of the γ-phase field with the four dual-phase alloys. This extension lay on a line of approximately constant *e*/*a* ratio, equivalent to assigning the ternary phase the stoichiometry $Al_4Au_xCu_{9-x}$ where $0<x<\sim6$. There is no classic γ-phase on the Al-Au edge with γ-

$AlAu_2$ (e/a=1.67 and the $MoSi_2$ structure) the best matching candidate, but has a different crystal structure to classic γ-phase. Therefore it is clear that the $Al_4Au_xCu_{9-x}$ phase cannot extend as far as the Al-Au edge and there must be a two-phase $Al_4Au_xCu_{9-x}$+$AlAu_2$ field in-between. In any case, at 750˚C the γ-phase only extends from 0 to ~40 at.% Au, beyond which the sample is molten, Figure 9(a). Examination of the quenched Sample 14, the bulk of which would comply with the stoichiometry $Al_4Au_6Cu_3$, showed that it consists of dendrites of β, interwined with dendrites of γ, surrounded finally by a eutectic of $AlAu_2$ and γ, Figure 9(b) and 9(c). The β-phase had decomposed during cooling to precipitate γ from a matrix that became slightly enriched in Au. From the liquidus and microstructure data it can be deduced that the eutectic composition must have been molten at the annealing temperature of 750˚C with a composition of 29.5 at%. Al and 31.0 at.% Cu, and that the eutectic itself must therefore have formed during the quench. Analysis of the β-phase indicated a composition of 27.0 at.% Al and 26.8 at.% Cu. Levey had reported β-phase in this general region too (but at 500˚C) , and examination of the original micrographs of Levey by the present authors showed that it too had decomposed on cooling, with precipitation of a needle-shaped laths of γ-phase. The present observations can be readily explained if it is noted that isopleths across β-phase regions are generally V-shaped, with the apex of the V at an e/a ratio of about 1.48. Therefore, on cooling β-phase samples tend to precipitate γ- or α-phase, depending on whether their e/a is >1.48 or < 1.48, respectively. Actually, the original data of Levey showed precipitates of γ in β-phase samples with as little as 5% Al, and here we have redrawn her 18 K isopleth to reflect this, Figure 9(d). The microstructures of Figure 9(b) and (c) can therefore be explained as follows. First, the melt in this region of the phase diagram passes into the L+β+γ field, forming interwined dendrites of β and γ. Then, as the remaining liquid becomes enriched in Al and the temperature falls further, a eutectic of γ+Al_2Au or γ+$AlAu_2$ (depending on actual starting composition, it was $AlAu_2$ for the present Sample 14) forms. Meanwhile, the dendrites of β shed a precipitate of γ as the temperature falls.

The remaining phase field, that of the Au-rich liquid, was drawn in by noting the melting points on the binary edges, the estimated liquidus temperatures of the Levey isopleth and the general trend of the Al_2Au+γ eutectic.

4. Conclusion

We have provided a general outline of the phases present in the Al-Cu-Au ternary diagram at 750 °C. An isothermal section was drawn using the observed data and microstructures. Interpolation of regions where there was little data was undertaken by applying the principles of ternary systems. The ternary β-phase of the Spangold alloy appears to be contiguous with that of Cu_3Al. It is likely that the entire range of β-phase compositions could serve as the basis of a shape-memory alloy. Transformation temperatures will be controlled by both e/a ratio and Au content. In particular, increase in the Au content brings down the transformation temperature, all else being equal. In addition, an increased content of Au stabilizes the β-phase too, and makes it resistant to decomposition at intermediate temperatures over technologically relevant timescales.

The other interesting attribute of this system is its ternary γ-phase, which extends deep into the isothermal section from the Al-Cu edge. Au substitutes for Cu in the structure of this compound, giving it a nominal stoichiometry of $Al_4Au_xCu_{9-x}$ where $0<x<\sim6$. The compound is not stable for $x> \sim6$ and in that case forms a two-phase microstructure with $AlAu_2$.

Acknowledgements

The authors thank Dr Norman Booth and Mr Jean-Pierre Guerbois, of the University of Technology Sydney, for technical assistance, and Drs F. Levey and I. Wolff (both formerly of Mintek, South Africa) for earlier contributions and discussions. Part of this research was undertaken on the Powder Diffraction Beamline at the Australian Synchrotron, Victoria, Australia. The views expressed herein are those of the authors and are not necessarily those of the owner or operator of the Australian Synchrotron.

References

[1] K. Otsuka, C. M. Wayman, Shape Memory Materials Cambridge University Press, Cambridge, 1999.
[2] I. M. Wolff, M. B. Cortie, The development of Spangold, Gold Bull. 27(2) (1994) 44-54.
[3] M. Sreekumar, T. Nagarajan, M. Singaperumal, M. Zoppi, R. Molfino, Critical review of current trends in shape memory alloy actuators for intelligent robots, Ind. Robot 34(4) (2007) 285-294.
[4] F. El-Feninat, G. Laroche, M. Fiset, D. Mantovani, Shape memory materials for biomedical applications, Adv. Eng. Mater. 4(3) (2002) 91-104.
[5] M. Es-Souni, H. Fischer-Brandies, Assessing the biocompatibility of NiTi shape memory alloys used for medical applications, Anal. Bioanal. Chem. 381(3) (2005) 557-567.
[6] C. D. J. Barras, K. A. Myers, Nitinol - Its use in vascular surgery and other applications, , Eur. J. Vasc. Endovasc. 19(6) (2000) 564-569.
[7] W. Cai, X. L. Meng, L. C. Zhao, Recent development of TiNi-based shape memory alloys, Curr. Opin. Solid. St. Mater. Sci. 9(6) (2005) 296-302.
[8] N. Suresh, U. Ramamurty, Aging response and its effect on the functional properties of Cu–Al–Ni shape memory alloys, J. Alloys Compd. 449(1-2) (2008) 113-118.
[9] N. F. Kennon, D. P. Dunne, L. Middleton, Aging effects in copper-based shape memory alloys, Metall. Trans. A 13(4) (1982) 551-555.
[10] P. Rodriguez, G. Guenin, Thermal aging behaviour and origin of a Cu-Al-Ni shape memory alloy, Mater. Sci. Eng., A 129(2) (1990) 273-277.
[11] Y. Murakami, S. Morito, Y. Nakajima, K. Otsuka, T. Suzuki, T. Ohba, Effect of aging zeta'2 martensite on the enthalpy of transformation in a Au-49.5 at. percent Cd alloy, Mater. Lett. 21(3-4) (1994) 275-278.
[12] A. Prince, G. V. Raynor, D. S. Evans, Phase Diagrams of Ternary Gold Alloys. The Institute of Metals, London, 1990.

[13] D. P. Morris, C. D. Price, J. L. Hughes, The Heusler structure of Au_2MnAl, Acta Cryst. 16 (1963) 839-839.
[14] S. Urbano, A. Manca, S. Besseghini, G. Airoldi, Martensite ageing effects in $Au_7Cu_5Al_4$, Scr. Mater. 52(4) (2005) 317-321.
[15] L. Fumagalli, S. Besseghini, F. Passarett, G. Airoldi, Thermoelastic martensitic transformation in Au-Cu-Al alloys doped with Co or Ir, J. Alloys Compd. 433 (2007) 332-337.
[16] M. Cortie, I. Wolff, F. Levey, S. Taylor, R. Watt, R. Pretorius, T. Biggs, J. Hurly, Spangold, a jewellery alloy with an innovative surface finish, Gold Technol. 14 (1994) 30-36.
[17] S. Besseghini, F. Passaretti, E. Villa, P. Fabbro, F. Ricciardi, Gold with a martensitic transformation: which opportunities?, Gold Bull. 40(4) (2007) 328-335.
[18] R. Shukla, V. Bansal, M. Chaudhary, A. Bas, R. R. Bhonde, M. Sastry, Biocompatibility of gold nanoparticles and their endocytotic fate Inside the cellular compartment: a microscopic overview, Langmuir 21 (2005) 10644-10654.
[19] C. C. Shih, C. M. Shih, K. Y. Chou, S. J. Lin, Y. Y. Su, Electrochemical and SEM characterization of gold-coated stents in vitro, J. Electrochem. Soc. 154 (2007) C326-C330
[20] F. C. Levey, M. B. Cortie, L. A. Cornish, A 500°C isothermal section for the Al-Au-Cu system, Metall. Mater. Trans. A. 33A (2002) 987-994.
[21] F. C. Levey, M. B. Cortie, L. A. Cornish, Determination of the 76 weight % Au section of the Al-Au-Cu system, J. Alloys Compd. 354 (2003) 171-180.
[22] J. L. Murray, Alloy Phase Diagrams. ASM Materials International, Materials Park, Ohio, 2002.
[23] M. B. Cortie, F. C. Levey, Structure and ordering of the 18-carat Al-Au-Cu β phase, Intermetallics 8(7) (2000) 793-804.
[24] N. R. Chapman, E. Gillam, Side-band formation in an ordered alloy, Acta Metall. 13 (1965) 434-436.
[25] M. B. Cortie, C. E. Mavrocordatos, The decomposition of the beta phase in the copper-tin system, Metall. Trans. A 22A (1991) 11-18.
[26] H. Warlimont, L. Delaey, Martensitic transformations in copper-, silver- and gold-based alloys, Prog. Mater. Sci. 18 (1974) 1-155.
[27] I. M. Wolff, Spangold: a new aura for intermetallics, Endeavour 19(1) (1995) 16-19.
[28] L. Battezzati, G. Fiore, M. Massazza, A shape memory gold alloy processed by rapid solidification, J. Alloys and Compounds 434/435 (2007) 264-267.
[29] F. C. Levey, M. B. Cortie, L. A. Cornish, Displacive transformations in Au - 18 wt% Cu - 6 wt% Al, Metall. Mater. Trans. A. 31A (2000) 1917-1923.

Table 1 Composition of annealed samples from averaged EDS results

	Total			Phase 1			Phase 2		
Sample Number	Al at%	Cu at%	Au at%	Al at%	Cu at%	Au at%	Al at%	Cu at%	Au at%
1	28.5	46.9	24.4						
2	28.8	48.3	22.8						
3	32.1	48.3	19.5	32.4	48.0	19.5	eutectic		
4	35.0	48.9	16.0	32.7	52.6	14.6	59.0	7.4	33.4
5	29.9	56.6	13.4						
6	15.1	54.9	29.9						
7	18.6	55.2	26.0	17.4	56.6	25.8	18.7	54.3	26.9
8	21.8	49.6	28.5						
9	24.7	47.2	28.0	25.8	46.1	27.9	24.1	47.5	28.2
10	20.9	35.7	43.3						
11	21.6	41.9	36.3						
12	24.4	65.9	9.6	23.0	67.5	9.3	27.6	62.1	10.2
13	23.1	76.8	0.0						
14	27.9	25.8	46.1	28.2	26.8	44.9			
two phase regions of 14 (overall)				27.0	26.0	46.9	29.6	19.5	50.8

Figure captions

Figure 1. Isothermal section for Al-Au-Cu system at 750˚C. (a) Superimposed data of present samples, binary edge data and 18 karat isopleth data. Probable two- and three-phase boundaries have been included for completeness but have not yet been directly verified. Tie-line between γ and Al_2Au shown as dotted line. Dashed line gives approximate locus of eutectic valleys around Al_2Au. (b) Simplified version of (a), showing only extent and identity of single phase fields.

Figure 2 The α-phase in Sample 6. (a) Optical micrograph showing dendrites of α in a lighter-etching matrix of α which was shown by SEM EDS to be enriched in both Al and Au. (b) Backscatter SEM image showing cored dendrites of α (darker grey) in an Au-enriched matrix. The last vestige of liquid to solidify has formed interdendritic inclusions of light-coloured β-phase.

Figure 3 Decomposition of the β-phase in Sample 7. (a) SEM backscatter image showing how Widmanstätten needles of α-phase precipitated in the β matrix as the as-cast sample cooled to room temperature. (b) Optical micrograph showing how a feathery non-ferrous bainite nucleated on the prior β grain boundaries when a β-phase sample was quenched from an annealing temperature of 750˚C. (c) Higher resolution SEM backscatter image of bainite (with enhanced contrast provided by image processing software) showing fine-scale domains of α in a matrix of residual β. (d) Optical micrograph showing dark-etching α in a matrix of β.

Figure 4. Optical microscopy using Nomarski interference contrast to show the transformation of the β-phase of Sample 10 to martensite. (a) Before the transformation showing a polished surface and (b) after the phase transformation showing raised laths.

Figure 5. Melting of the β-phase. (a) Melting points obtained from DTA measurements and from literature. The 750˚C isotherm is intersected at about 47 at.% Au. (b) Portion of X-ray diffraction patterns obtained *in situ* using synchrotron radiation showing {011} peak; patterns have been offset for easy visualisation. (c) Integrated intensity of {011} peak as a function of temperature showing how sample melted between 740 and 800˚C. Onset of melting is indicated in the decline in peak intensities at temperatures at approximately 730˚C.

Figure 6. (a) Differential scanning calorimetry traces taken from three β-phase compositions, showing the austenite and martensite transformations. (b) Effect of Au on the A_p temperatures of Al-Au-Cu β-phase in the range 30 to 60 at% Au. Solid symbols are from the work of Fumagalli et al.[15], the open symbols are from the present work. The line is drawn merely to guide the eye.

Figure 7. (a) Indicative X-ray diffraction patterns from these γ-phase samples are given for Samples 1 and 5 and compared with a JCPDF entry for Al_4Cu_9. (b) Lattice parameter, *a*, for γ-phase as a function of Au content. Solid symbols- present work, empty squares from Levey [20], crossed square from JCPDF database, card number 24-3.

Figure 8. (a) SEM backscatter micrograph of $AuAl_2$+γ microstructure of Sample 4 in the as-cast state showing some tendency towards formation of an 'abnormal' eutectic (b) Thermal analysis curves (cooling) showing formation of γ followed by γ + $AuAl_2$ eutectic. (c) SEM backscatter micrograph of $AuAl_2$+γ microstructure of Sample 4 in the solution annealed and quenched state showing how the eutectic has spheroidised. (d) Dual phase (γ+β) microstructure of Sample 9.

Figure 9. (a) Melting point of γ-phase as a function of Au content. (b) SEM backscatter image showing how Sample 14 solidified first as dendrites of γ and β, before forming an Au- and Al-rich eutectic. (c) Higher magnification image of Sample14 showing that its eutectic was comprised of γ and $AlAu_2$ and that its β-phase dendrites formed extensive precipitates of γ upon further cooling. (d) Updated and corrected 18 karat isopleth through Al-Au-Cu ternary system, redrawn after Levey et al.[21] with corrected β/(γ+β) phase boundaries.

Figures

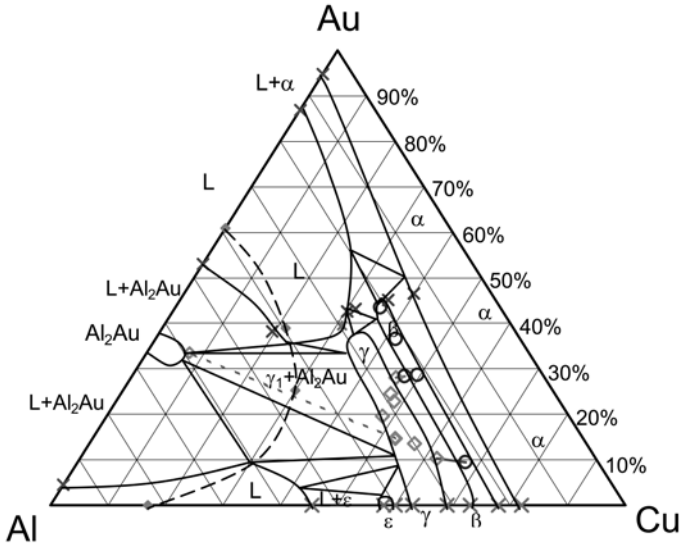

a

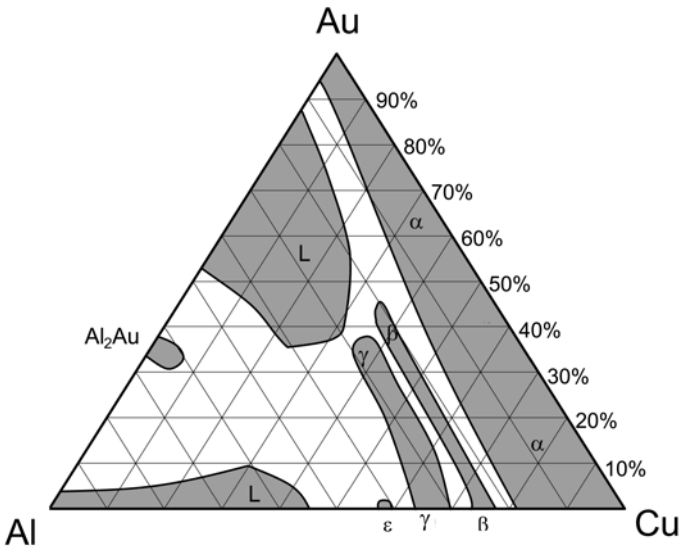

b

Figure 1

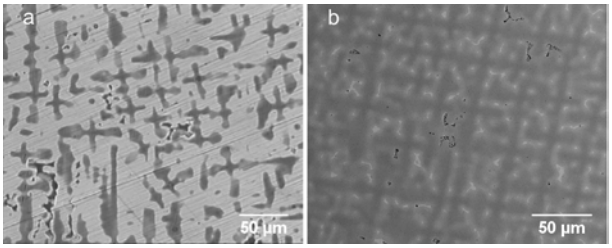

Figure 2

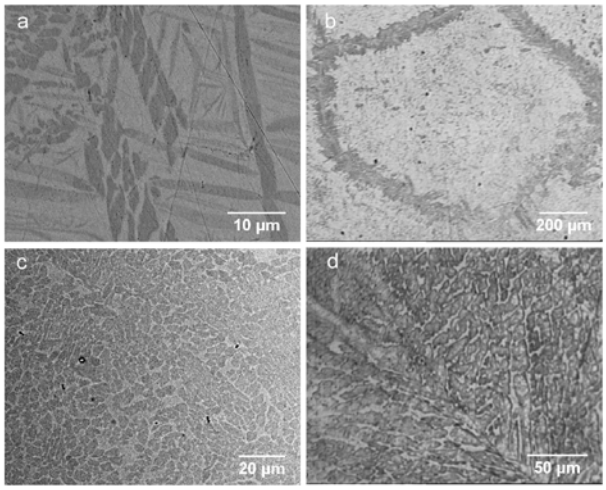

Figure 3

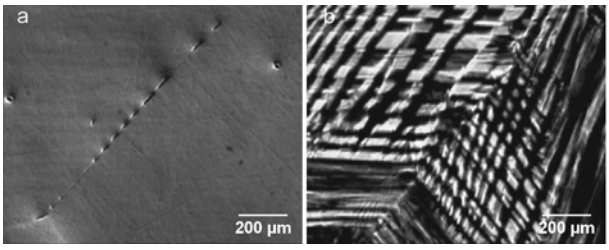

Figure 4

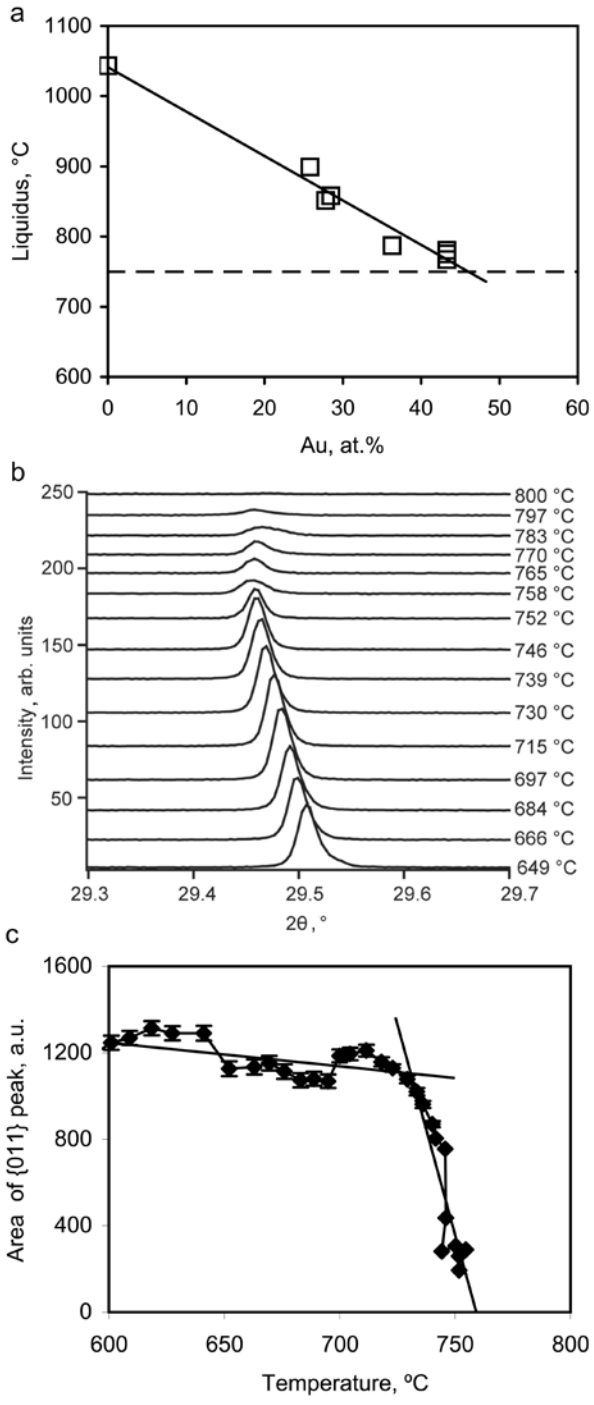
a
1100
1000
900
800
700
600
Liquidus, °C
0
10
20
30
40
50
60
Au, at.%
b
250
200
150
100
50
Intensity, arb. units
800 °C
797 °C
783 °C
770 °C
765 °C
758 °C
752 °C
746 °C
739 °C
730 °C
715 °C
697 °C
684 °C
666 °C
649 °C
29.3
29.4
29.5
29.6
29.7
2θ, °
c
1600
1200
800
400
0
Area of {011} peak, a.u.
600
650
700
750
800
Temperature, ºC

Figure 5

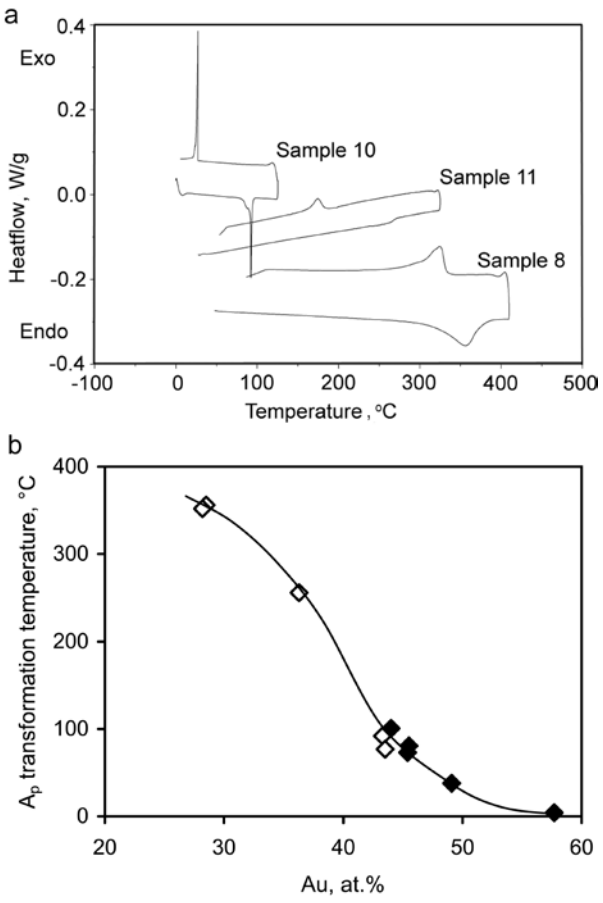
a
Exo
Endo
Heatflow, W/g
Temperature , °C
Sample 10
Sample 11
Sample 8
b
A_p transformation temperature, °C
Au, at.%

Figure 6

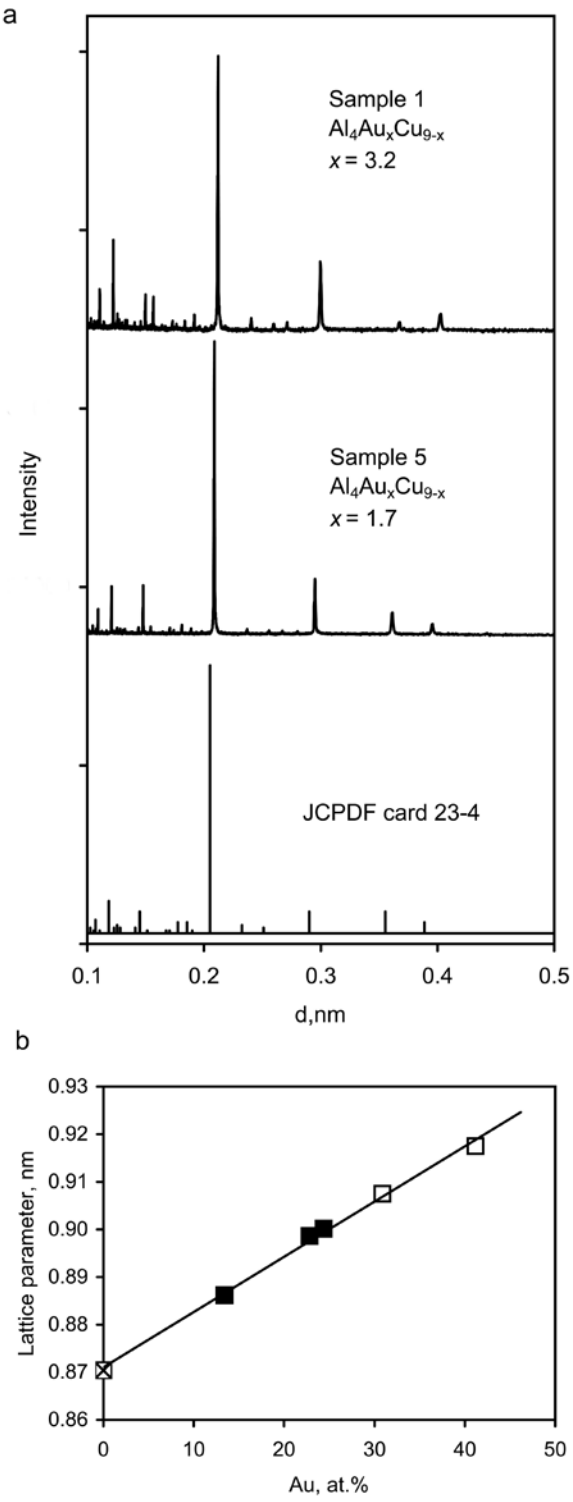
a
Sample 1
Al4AuxCu9-x
x = 3.2
Sample 5
Al4AuxCu9-x
x = 1.7
JCPDF card 23-4
Intensity
0.1
0.2
0.3
0.4
0.5
d,nm
b
Lattice parameter, nm
0.93
0.92
0.91
0.90
0.89
0.88
0.87
0.86
0
10
20
30
40
50
Au, at.%

Figure 7

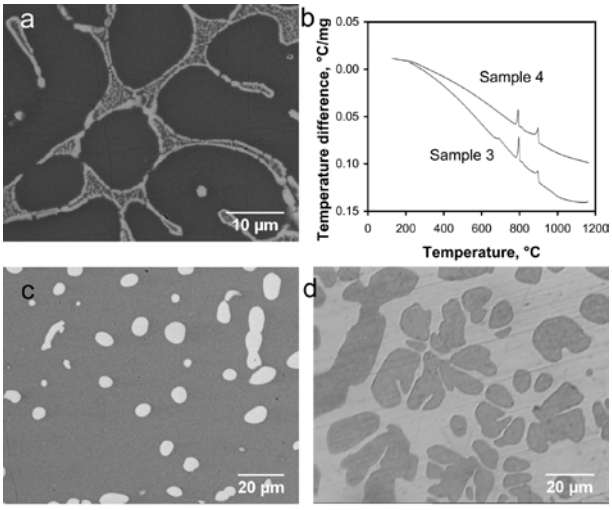
a
10 µm
b
Temperature difference, °C/mg
0.05
0.00
0.05
0.10
0.15
Sample 4
Sample 3
0
200
400
600
800
1000
1200
Temperature, °C
c
20 µm
d
20 µm

Figure 8

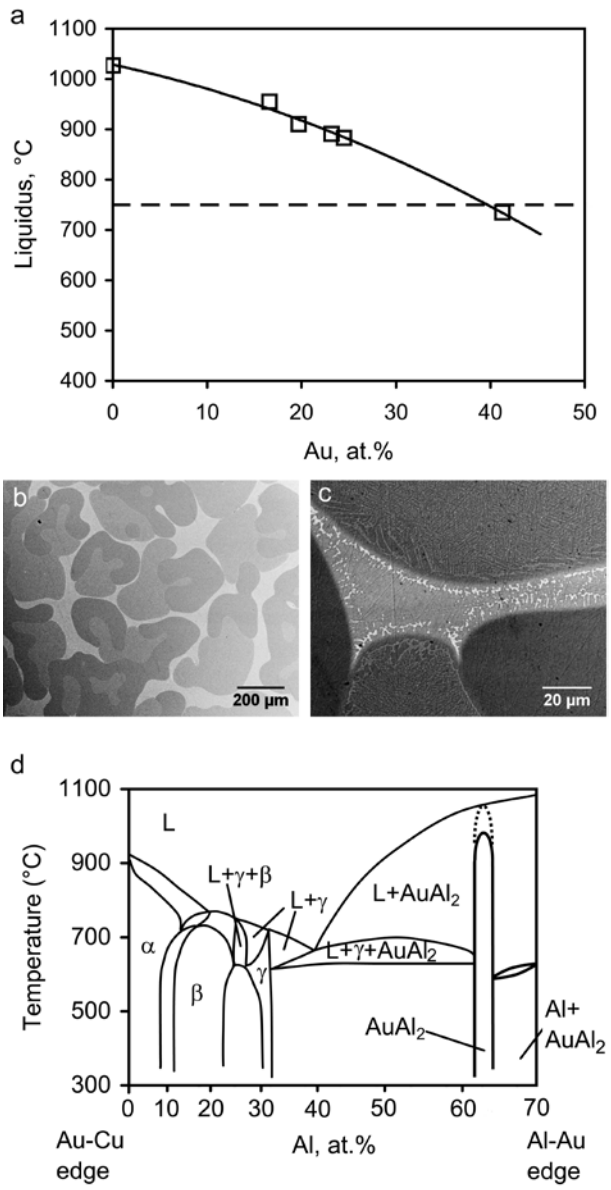
a
Liquidus, °C
Au, at.%
b
200 µm
c
20 µm
d
Temperature (°C)
L
L+γ+β
L+γ
L+AuAl2
L+γ+AuAl2
α
β
γ
AuAl2
Al+
AuAl2
Au-Cu
edge
Al, at.%
Al-Au
edge

Figure 9